


RESEARCH

Open Access



Pulsed polarized vortex beam enabled by metafiber lasers

Chenxi Zhang^{1†}, Lei Zhang^{2,3,4†}, He Zhang¹, Bo Fu^{1,5*} , Jiyong Wang^{6*} and Min Qiu^{2,3,7*}

[†]Chenxi Zhang and Lei Zhang contributed equally to this work.

*Correspondence:

fubo10@buaa.edu.cn;
jiyongwang@hdu.edu.cn;
qiumin@westlake.edu.cn

¹ Key Laboratory of Precision Opto-Mechatronics Technology of Education Ministry, School of Instrumentation and Optoelectronic Engineering, Beihang University, Beijing 100191, China

² Key Laboratory of 3D Micro/Nano Fabrication and Characterization of Zhejiang Province, School of Engineering, Westlake University, 18 Shilongshan Road, Hangzhou 310024, Zhejiang Province, China

³ Institute of Advanced Technology, Westlake Institute for Advanced Study, 18 Shilongshan Road, Hangzhou 310024, Zhejiang Province, China

⁴ QianYuan National Laboratory, Hangzhou 310000, China

⁵ Key Laboratory of Big Data-Based Precision Medicine Ministry of Industry and Information Technology, School of Engineering Medicine, Beihang University, Beijing 100191, China

⁶ Ministry of Education Engineering Research Center of Smart Microsensors and Microsystems, School of Electronics and Information, Hangzhou Dianzi University, Hangzhou 310018, China

⁷ Westlake Institute for Optoelectronics, Fuyang, Hangzhou 311421, China

Abstract

Pulsed polarized vortex beams, a special form of structured light, are generated by tailoring the light beam spatiotemporally and witness the growing application demands in nonlinear optics such as ultrafast laser processing and surface plasma excitation. However, existing techniques for generating polarized vortex beams suffer from either low compactness due to the use of bulky components or limited controlment of pulse performance. Here, an all-fiber technique combining plasmonic metafibers with mode conversion method is harnessed to generate high-performance pulsed polarized vortex beams. Plasmonic metafibers are utilized as saturable absorbers to produce Q-switched pulses with micro-second duration, while the offset splicing method is employed to partially convert the fundamental transverse mode (LP_{01}) to higher-order mode (LP_{11}). Eventually, a polarized vortex beams laser is achieved at the telecom band with a repetition frequency of 116.0 kHz. The impact of geometrical parameters including period of metafibers and offset of splicing on the spatiotemporal properties of pulsed polarized vortex beams is systematically investigated. Our findings could pave the way for design, control and generation of all-fiber pulsed polarized vortex beams, and also offer insights into the development of other types of structured laser sources.

Keywords: Metafiber, Q-switched pulse, Polarized vortex beam

Introduction

Vortex light is a spatially structured beam with a helical wavefront, characterized by a circular spatial intensity distribution and carrying orbital angular momentum [1, 2]. These unique spatial properties have fueled research in various fields, including quantum information, super-resolution microscopy and optical tweezers, to name a few [3–5]. Within the scope of vortex beam, polarized vortex beams (PVBs), also commonly termed as cylindrical vector beams, have been widely used in both basic research and practical applications due to the special polarization distribution [1, 6]. According to the spatial distribution of polarization, PVBs can be classified as a radially polarized beam (TM_{01}), an azimuthally polarized beam (TE_{01}), and a hybridly polarized beam ($HE_{21}^{\text{even/odd}}$) [7–9]. In particular, radially polarized beam can be focused into a tight spot with strong longitudinal field confinement, thus further promoting applications in high-resolution imaging, nanoparticle manipulation, plasma

focusing, and Z-scanning techniques [10–12]. The generation of PVBs routinely involves techniques such as axial birefringent assemblies [13, 14], spatial light modulators [15, 16], and nanostructured holograms with high efficiency and high power [17, 18]. Nevertheless, these methods consist of discrete bulky components, thus posing challenges in constructing compact, low-loss, and long-haul systems due to the complexities of optical alignment [19]. Conversely, all-fiber methods based on mode conversion theory provide an alternative approach for developing PVBs with greater flexibility and compactness [7, 20]. For instance, long period fiber grating and mode selective coupler have been well developed for transforming the fundamental mode into PVBs with high modal purity [21–24]. In comparison, offset splicing (OSS) which requires less stringent control of geometric parameters of the fiber, also serves as a simpler and effective approach to generate PVBs [7, 25].

On the other hand, the operational accuracy and resolution of vortex light are closely linked to its temporal-domain properties. Tailoring the PVBs in temporal domain to form pulsed PVBs, which have been employed in various applications, such as ultrafast laser processing, surface plasma excitation, and other nonlinear light-matter interactions [26, 27]. Converting the fundamental mode of pulsed laser into higher-order mode is essential to generate the pulsed PVBs [28–31]. Consequently, saturable absorbers (SAs) have garnered significant attention due to their practicality and superior effectiveness in generating Q-switched and mode-locked pulses in solid-state and fiber lasers [32–37]. Pioneering study integrated plasmonic nanorod metasurface on the fiber end facets to form the plasmonic metafibers as SAs, resulting in pulsed lasers at designable wavelengths [38]. Benefitting from well-defined shapes, sizes and geometries of the unit cell, plasmonic metafibers exhibiting outstanding saturable absorption closely related to the plasmonic resonances [39–41]. However, the resonance of such nanorod metasurface exhibits a strong dependence on polarization. Therefore, pulsed lasers are highly sensitive to environmental vibration and other disturbances. Additionally, the resonance-shift-based saturable absorption is constrained by the wide full width at half maximum due to the intrinsic ohmic and radiative losses [42]. Alternatively, metasurfaces with centrosymmetric shapes, such as nanorings and nanoeyes integrated on the fiber tips have been demonstrated to support polarization-independent and sharp resonances for sensing and modulation [39, 43, 44]. However, the effective utilization of plasmonic metafibers to deliberately structure light in terms of both polarization and pulse properties, while accounting for spatiotemporal aspects, continues to pose a significant challenge.

In this work, we demonstrate a Q-switched pulsed PVB that features a micro-second pulse duration by in collaborating polarization-independent metafibers with the simple and efficient OSS technique. As shown in Fig. 1, the unit cell of metafiber is the so-called nanoeye structure [39, 44], situated in the core region of a commercial single-mode fiber jumper (SMFJ) for plug-and-play operations. The metafiber is used as a SA for the generation of Q-switched pulses. The output port of the single-mode fiber (SMF) is offset spliced with a two-mode fiber (TMF) to partially convert the fundamental transverse mode (LP_{01}) to higher-order mode (LP_{11}), and the pulsed vortex laser is eventually achieved at the telecom band. The impact of geometric parameters involving the periods

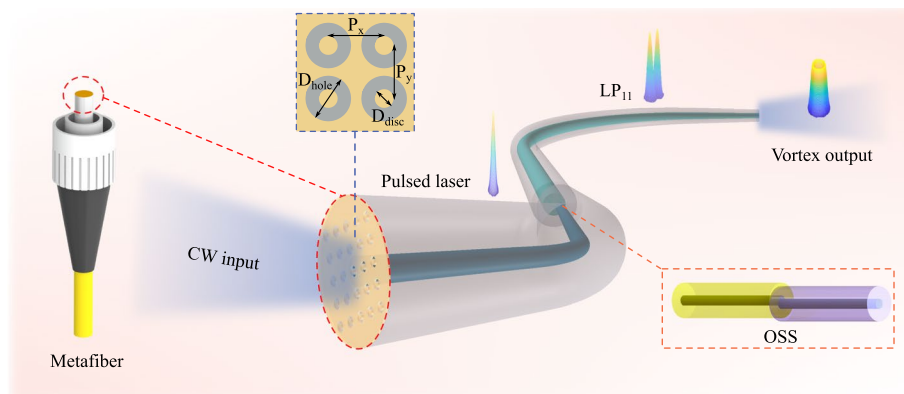


Fig. 1 Configuration and working principle of the generation of pulsed polarized vortex beam

of nanoeye in the metafibers and offset of splicing on the spatiotemporal characteristics of pulsed PVB is respectively investigated. This study enhances our understanding of the role of metasurfaces in beam manipulation, and paves the way for the generation of all-fiber structured lights.

Results and discussion

Optical responses of metafibers

As shown in Fig. 1, the plasmonic nanoeye metasurfaces are situated in the core region of SMFJ to form the metafiber. The nanoeye structure is chosen as the unit cell of the plasmonic metasurfaces due to its extensive study [39, 43, 44]. The nanoeye can provide hybridized plasmonic modes stemming from coupling of individual nanodisc and nanohole modes, which greatly enhance light-matter interactions [39, 43, 44].

To characterize the optical responses of metafibers, four samples are fabricated with the period ranging from 825 nm to 900 nm in a step of 25 nm (see details of “Fabrication” from Method). The reflectance spectra of metafibers are investigated as functions of the period and incident wavelength, as shown in Fig. 2a. Three dips and two peaks are observed in the observation window for all periods. The broader resonance dips centered at 1430 nm, 1450 nm, 1490 nm and 1550 nm correspond to the bonding mode [39, 43]. Theoretical reflectance spectra and electric field distributions are calculated (see details of “Simulation” from Method). As shown in the inset of Fig. 2a, the electric field is strongly confined at the edged surfaces of the nanodisc with an orientation parallel to the polarization of incident light. Besides, at the reflectance spectra of 1550 nm, the reflectance intensity exhibits a monotone decreasing trend as the period increases.

Following the linear optical characterization, the nonlinear transmittance is further measured by using a home-made setups for saturable absorption characterization (central wavelength: 1550 nm, pulse width: 2 ps, and frequency: 20 MHz, see details of “Experimental setups for optical response characterization” from SI). As the input power continuously increases, the transmittance spectra for metafibers of all periods show the typical line shape of saturable absorption with the saturable power of 1.44 MW/cm^2 , as

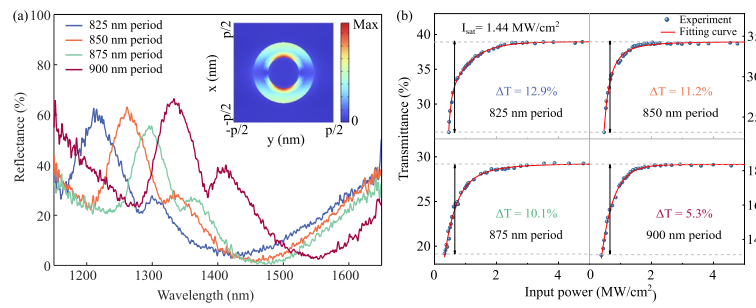


Fig. 2 Linear and nonlinear optical characterizations of plasmonic metafibers with the periods ranging from 825 nm to 900 nm in a step of 25 nm. **a** Reflectance spectra of metafibers. The inset is the electric field distribution at x-y plane for the plasmonic bonding mode excited at 1600 nm. **b** Optical transmittances of metafiber using a power-variable pulsed laser

shown in Fig. 2b. The transmittance exhibits a similar dependence on the period as the linear excitation, with the maximum modulation depth reaching up to 12.9%. The modulation depth of metafiber is higher compared with that of the conventional SAs, which facilitates the low saturation intensity pulse modulation [28, 29, 32].

Generation of Q-switched pulse lasers

Based on the optical responses of metafibers, we design a passively all-fiber laser cavity to acquire the Q-switched pulses, as shown in Fig. 3a. The laser cavity consists of a pump diode (980 nm), a polarization-independent optical integrated module (PI-OIM), an erbium-doped gain fiber (EDF, 0.7 m), a polarization controller (PC), and a metafiber SA with the period of 825 nm. The PI-OIM can effectively reduce the loss and maintain the total length less than 1 m. The inset depicts a well-defined plasmonic nanoeye structure situated in the core region. The high precision ensures the propagation of light and promotion a stable build-up of Q-switched laser. Figure 3b depicts the spectrum of the Q-switched pulse laser with the central wavelength of 1559.0 nm. A broader full width at half maximum of 1.3 nm is obtained by using the metafiber SA, better than other Q-switched pulses generated by the traditional SAs [28, 29, 32]. Figure 3c shows a pulse train of the laser with an interval of 8.6 μ s, corresponding to the repetition frequency of 116.0 kHz. The RF spectrum shown in Fig. 3d displays that 40 dB signal-to-noise ratio of the fundamental frequency can be reached. The pulse width of the Q-switched laser is 1.0 μ s as shown in Fig. 3e. To compare the improved performance of metafiber SAs with traditional SAs, we select four types of SAs, including zero-dimensional, one-dimensional, two-dimensional materials and our metafibers. (See details of “Performance comparison between metafiber SAs and traditional SAs” from SI) Metafiber SAs exhibit superior performance Q-switched threshold, repetition frequency and pulse width. Specifically, metafibers SAs show a generally low threshold which reduces potential thermal damages and promotes the energy conversion efficiency [45]. Besides, a high repetition frequency from metafiber SAs is preferred for the data transmission in the field of high speed communication network [46].

Further, we systematically investigate the impact of pump power and period of metafiber on the output characteristics of Q-switched lasers. Figure 4a, b show dependences of pulse width, repetition frequency, pulse energy and peak power on pump power. As the pump power increases, the pulse width exhibits a decrease trend to a minimum of 1.0 μ s, while

the repetition frequency, pulse energy and peak power increase to 116.0 kHz, 16.6 nJ and 17.5 mW, respectively. Figure 4c displays that the laser has a low Q-switched threshold of 35 mW and a maximum output power of 2 mW. The output characteristics of Q-switched pulse laser are closely related to the pump power, which is maximized to 190 mW under the condition of intact stability of metafibers.

Subsequently, we compare the pulse characteristics of the Q-switched lasers as functions of the periods of metafiber. As shown in Fig. 4d, e, we find that pulse width, repetition frequency, output power, pulse energy and the lateral diameter of pulse pattern all deteriorate as the periods of metafiber increase. This negative correlation can be attributed to two folds of reasons. First, the resonance enhanced absorption becomes remarkable when the resonance wavelength shifts to a longer wavelength with the period (cf. Fig. 2a), resulting in an increase in total loss of the laser cavity during the linear absorption stage. Second, the modulation depth decreases with the periods (cf. Fig. 2b), leading to the deterioration of the pulse qualities during the nonlinear absorption stage. As a result, the increase in period of

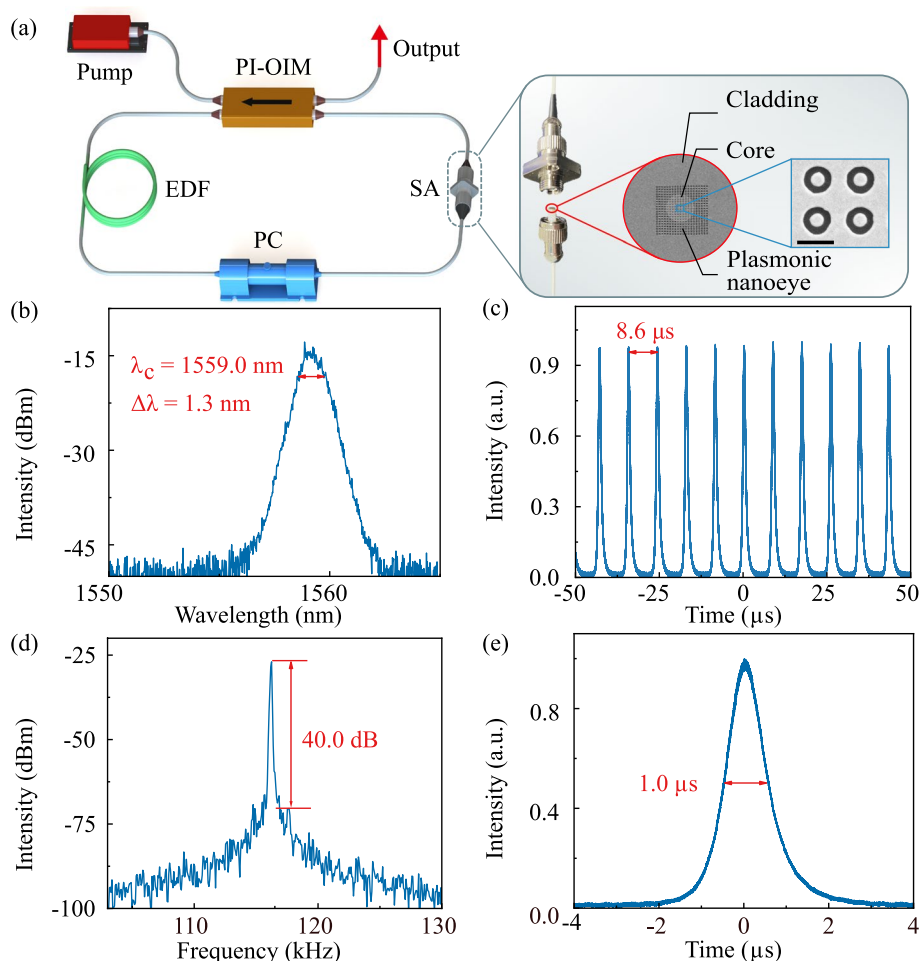


Fig. 3 Output characteristics of Q-switched pulsed lasers by using metafiber SA under 190 mW pump power. **a** Schematic diagram of laser setup. Inset is the optical image of a metafiber. The scale bar represents 825 nm. **b** Spectrum of Q-switched pulses with a central wavelength of 1559.0 nm. **c** Oscilloscope trace of the Q-switched pulses with a pulse interval of 8.6 μ s. **d** The RF spectrum of the output pulse train at a repetition rate of 116.0 kHz. **e** Single pulse profile with a duration of 1.0 μ s

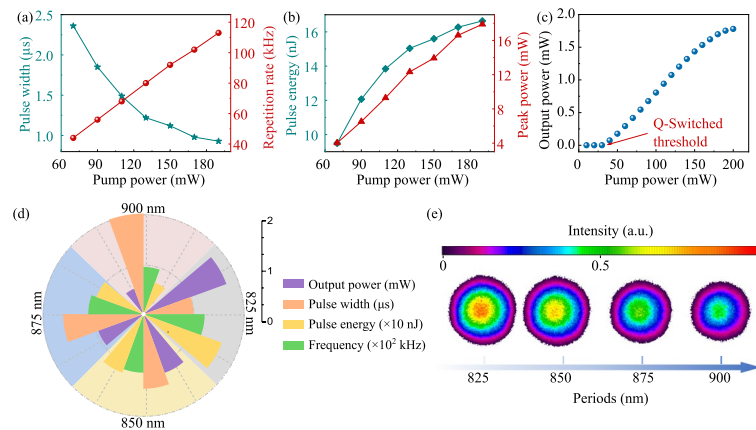


Fig. 4 Impact of pump power and period of metafiber on the pulse characteristics. **a** Pulse width and repetition rate versus pump power. **b** Pulse energy and peak power versus pump power. **c** Averaged output power versus pump power. **d** Output characteristics of Q-switched pulses versus periods of metafiber. **e** Spot pattern versus periods of metafiber

metafiber results in the deterioration of pulse qualities, hindering the generation of higher-order solitons and the subsequent pulsed PVB.

Generation and regulation of pulsed vortex beams

The number of propagation modes is determined by the normalized frequency parameter V in the transmission fiber, and V is formulated according to

$$V = \frac{2\pi\alpha}{\lambda} \sqrt{n_{\text{core}}^2 - n_{\text{cladding}}^2}, \quad (1)$$

where λ is the incident laser wavelength, α is the core radius, n_{core} and n_{cladding} are the refractive indexes of fiber core and cladding, respectively [47, 48]. When V is less than 2.405, the LP_{01} mode is supported in the fiber. When V lies between 2.405 and 3.832, the light wave excites LP_{11} ($HE_{21}^{\text{even/odd}}$, TE_{01} , TM_{01}) modes. Higher-order modes are excited when V exceeds 3.832. Since the SMF has a normalized V of 2.27, smaller than 2.405, only the fundamental mode of LP_{01} is allowed. The TMF utilized in the experiment has a core radius of 7 μm, and a step index difference of 0.005, corresponding to $V = 3.42$ at the incident wavelength of 1550 nm, fulfilling conditions for the excitation of the LP_{11} mode. The effective refractive indices of the TM_{01} and TE_{01} modes in LP_{11} mode display a slight variation when the polarization distribution is taken into account. To excite the fundamental mode to higher-order mode, a critical technology is employed, that is lateral OSS. By staggering and fusing the SMF and TMF together, higher-order mode can be effectively excited. According to mode coupling theory, for a horizontal polarized input (HE_{11}^x), the coupling efficient of HE_{11}^x to TM_{01} is dominant, while for a vertical polarized input (HE_{11}^y), the TE_{01} is manifested [49]. Thus, the TM_{01} modes can be selectively excited in the TMF by adjusting the input polarization state using PC_1 prior to the OSS point, thereby making the LP_{11} mode radially polarize only.

Through OSS, the fundamental mode of Gaussian profile can be converted to a higher-order mode and propagates in the TMF, as shown in Fig. 5a. Additionally, the PC_2 external

to the cavity is added to stabilize the operation state when the output port is moved in the optical table. The coupling efficiency is determined by the OSS configuration and the overlap of electric field distribution of waveguided modes in SMF and TME, which follows the equation:

$$\gamma_c = \left[\frac{4n_{\text{eff},1}n_{\text{eff},2}}{(n_{\text{eff},1} + n_{\text{eff},2})^2} \right] \left| \frac{\iint_{\infty} E_1(x,y)E_2^*(x,y)dx dy}{\sqrt{\iint_{\infty} E_1(x,y)E_1^*(x,y)dx dy \times \iint_{\infty} E_2(x,y)E_2^*(x,y)dx dy}} \right|^2, \quad (2)$$

where $E_1(x,y)$ and $E_2(x,y)$ are the electric fields of waveguide mode in the SMF and TME, respectively, and $n_{\text{eff},1}$ and $n_{\text{eff},2}$ are the corresponding effective refractive indices [5, 7, 9]. Figure 5b illustrates the relationship between coupling efficiency and the offset (ΔR) of splicing. As ΔR increases, the coupling efficiency initially rises to its maximum value of above 25%. Beyond this point, the coupling efficiency subsequently decreases due to the loss of the fundamental mode optical field. This decrease in efficiency continues until the cores are completely misaligned, resulting in the disappearance of the optical field. As shown in Fig. 5c, the transmission spectra of the LP₀₁ and LP₁₁ modes at $\Delta R = 4.5 \mu\text{m}$ reveal the presence of a loss peak point at $1.557 \mu\text{m}$ within the LP₁₁ mode. Notably the transmission spectra of LP₀₁ and LP₁₁ modes are not complementary, which is attributed to the mode coupling efficiency and the mode propagation characteristic [50, 51]. These peaks also reflect the point of the interference extremum and the superposition of energy. Figure 5d shows the intensity distributions of the LP₀₁ and LP₁₁ modes at offsets of 0 and $4.5 \mu\text{m}$. Under the condition of OSS ($\Delta R = 4.5 \mu\text{m}$), the LP₀₁ mode light instantly excites the LP₁₁ mode. They then propagate in the TME and interfere with each other. This interference leads to the presence of an extreme value of energy intensity, display as a superposition or attenuation of the energy in the TME, which is further supported by the spectrum (see details of “Detection of multimode interference based on OSS configuration” from SI). As shown in Fig. 5e, f, extremely bright spots can be observed in waveguide mode field when the offset is 0 and $4.5 \mu\text{m}$. A relatively low light field distribution can also be observed within the cladding layer aside the OSS point, which results from the strong interference.

The intensity of the pulse exerts a profound influence on the efficiency, quality, and stability of the subsequent pulsed PVBs generation, especially for the mode conversion method. A high pulse intensity is necessary to surpass the threshold for the generation of pulsed PVBs [52]. Therefore, the Q-switched pulsed laser generated by the metafiber SA of 825 nm is chosen since it has the highest pulse intensity. To analyze the polarization state of the pulsed PVB, the ΔR is kept as $4.5 \mu\text{m}$, and a linear polarizer is sandwiched between the pulsed PVB source and the CCD that monitors the spot profiles, as shown in Fig. 6a. As shown in Fig. 6b, c, spot profiles of the pulsed PVBs exhibit donut-like patterns with partially eccentric intensity distributions. The non-uniform spot intensity arises from the existence of residual fundamental mode components within the beam, which consequently reduces the purity of both TE₀₁ and TM₀₁ modes. Although, the spot pattern can still be divided into four different polarized directions after passing through the linear polarizer. The direction of the passing light rotates in accordance with the transmission axis of the

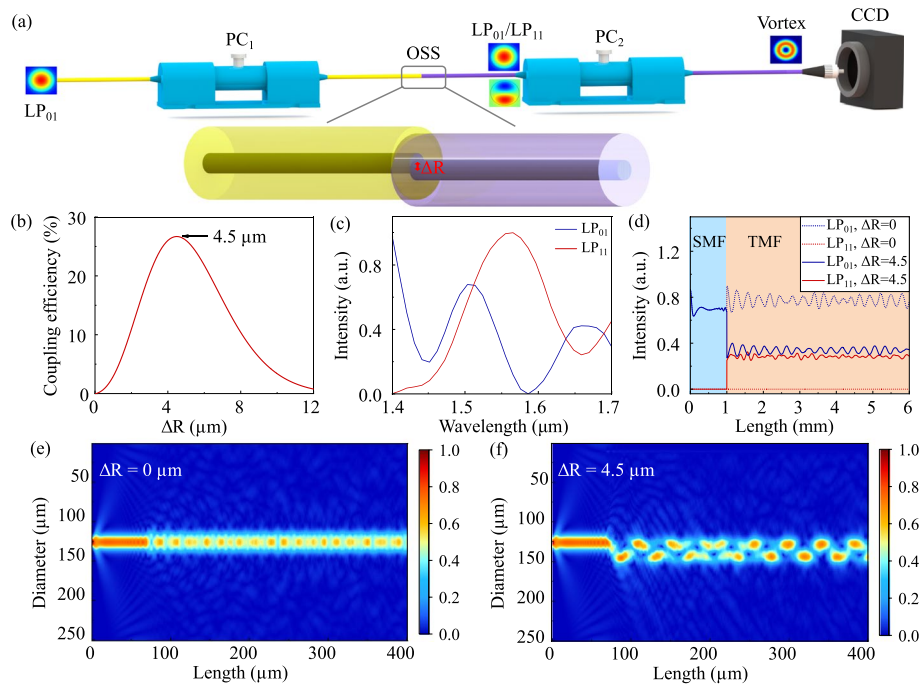


Fig. 5 Mechanism of pulsed PVB generation. **a** Diagram of the device for all-fiber vortex beam generation. **b** Coupling efficiency of OSS versus offset ΔR . **c** Transmission spectra of LP_{01} and LP_{11} with a ΔR of 4.5 μm . **d** Intensity distributions of LP_{01} and LP_{11} modes at different points of the fiber. **e, f** Waveguide mode field power transmission when the offset is 0 and 4.5 μm

polarizer. In Fig. 6b, the dark band is consistently perpendicular to the transmission axis of the polarizer, indicating the nature of this pulsed PVB is radially polarized. Alternatively, an azimuthally pulsed PVB can also be achieved by adjusting the PC_1 prior to the OSS point, where the dark band is consistently parallel to the transmission axis of the polarizer, as seen in Fig. 6c. In our future work, a direct integration of a spatiotemporal metasurface [36], which has a large modulation depth and phase control capability, onto the facet of multi-mode fibers may pave the way for the development of miniaturized laser sources with tailored spatial and temporal profiles.

Methods

Simulation The reflectance spectra and electric field distributions of the metafiber are simulated by using the three-dimensional finite element methods (COMSOL Multiphysics 6.0). The diameters of the inner nanodisc and outer nanohole are 280 nm and 550 nm, respectively. The thickness of the nanoeYE metasurface is 55 nm, while the period of the unit cell is swept from 750 nm to 900 nm in the step of 5 nm.

Fabrication Following the simulation, the metafiber is fabricated by using the advanced nanofabrication methods developed in our previous study [38, 39]. The thickness of gold film is 55 nm, consistent with the simulation setting. FIB (30 kV, 10 pA, Ga^+) is employed to precisely pattern the nanoeYE metasurface with the period ranging from

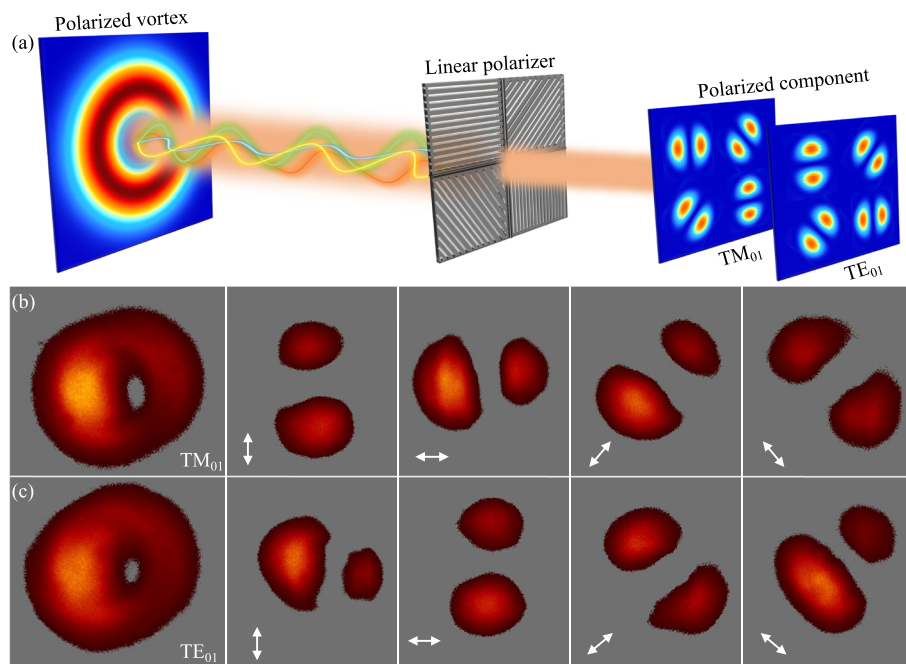


Fig. 6 Characterization and detection of pulsed PVBs. **a** Schematic of detection setups. **b, c** TM_{01} and TE_{01} vortex beam intensities and the direction of transmission after passing through the polarizer. The white arrow indicates the direction of each polarizer

825 nm to 900 nm in the step of 25 nm (see details of “Simulation and fabrication of plasmonic metafibers” from SI).

Characterization The linear reflectance spectra of the metafibers are measured by using the all-fiber reflectance testing system. The light source is selected as an SCL (operating wavelengths: 400–2400 nm). The metafiber is connected with the SCL and the OSA by a 50:50 fiber coupler, which can introduce the light to the metafiber and interrogate the reflectance signal. The optical signal is detected by the OSA (operating wavelengths: 650–1700 nm).

Conclusion

In conclusion, we have proposed and demonstrated an efficient scheme for generating pulsed PVBs using an all-fiber technique that incorporates plasmonic metafibers combined with a mode conversion method. Leveraging the plasmonic property of metafibers, a superior SA with a maximum modulation depth of 12.9% is obtained, enabling the generation of Q-switched pulses. The OSS method is used to partially convert the fundamental mode into the higher-order mode to obtain PVBs with microsecond pulse duration and 116.0 kHz repetition frequency. A quantitative regulation of the spatiotemporal properties of pulsed PVBs by tuning the periods of metafibers and offset of splicing is built and given. This work not only promotes in-depth research on the metafibers in the field of ultrafast optics, but also enhances their utility in spatially structuring light for the next generation of ultrafast pulsed laser source.

Supplementary Information

The online version contains supplementary material available at <https://doi.org/10.1186/s43074-024-00151-6>.

Supplementary Material 1. The preparation and characterization of the metafiber and its used as a saturable absorber to generate Q-switched pulses in comparison with traditional materials are given as supplementary information.

Acknowledgements

We thank Westlake Center for Micro/Nano Fabrication for the facility support and technical assistance.

Authors' contributions

M.Q. and B.F. lead the whole research project. C.Z., L.Z., J.W. and B.F. conceived the project. C.Z. performed the laser part. L.Z. performed the metafiber part. C.Z., L.Z., H.Z., B.F., J.W. and M.Q. analyzed the data and wrote the original manuscript.

Funding

This work was supported by the National Natural Science Foundation of China (Grant No. 62071016), the State Key Laboratory of Advanced Optical Communication Systems and Networks, China, and College Students Innovative Entrepreneurial Training Plan Program.

Data availability

The data that support the findings of this study are available from the corresponding author upon reasonable request.

Declarations

Competing interests

The authors declare no competing interests.

Received: 21 August 2024 Revised: 20 October 2024 Accepted: 25 October 2024

Published online: 04 November 2024

References

1. Mao D, Zheng Y, Zeng C, Lu H, Wang C, Zhang H, et al. Generation of polarization and phase singular beams in fibers and fiber lasers. *Adv Photon*. 2021;3(1):014002.
2. Wan Z, Wang H, Liu Q, Fu X, Shen Y. Ultra-degree-of-freedom structured light for ultracapacity information carriers. *ACS Photon*. 2023;10(7):2149–64.
3. Wang H, Zhan Z, Hu F, Meng Y, Liu Z, Fu X, et al. Intelligent optoelectronic processor for orbital angular momentum spectrum measurement. *PhotonIX*. 2023;4(1):9.
4. Huo P, Chen W, Zhang Z, Zhang Y, Liu M, Lin P, et al. Observation of spatiotemporal optical vortices enabled by symmetry-breaking slanted nanograting. *Nat Commun*. 2024;15(1):3055.
5. Lipson M. Guiding, modulating, and emitting light on silicon—challenges and opportunities. *J Light Technol*. 2005;23(12):4222–38.
6. Gui L, Wang C, Ding F, Chen H, Xiao X, Bozhevolnyi SI, et al. 60 nm span wavelength-tunable vortex fiber laser with intracavity plasmon metasurfaces. *ACS Photon*. 2023;10(3):623–31.
7. Mao D, Feng T, Zhang W, Lu H, Jiang Y, Li P, et al. Ultrafast all-fiber based cylindrical-vector beam laser. *Appl Phys Lett*. 2017;110(2):021107.
8. Dong Z, Zhang Y, Li H, Tao R, Gu C, Yao P, et al. All-fiber cylindrical vector beams laser based on the principle of mode superposition. *Opt Laser Technol*. 2021;139:106965.
9. Jocher C, Jauregui C, Becker M, Rothhardt M, Limpert J, Tünnermann A. An all-fiber Raman laser for cylindrical vector beam generation. *Laser Phys Lett*. 2013;10(12):125108.
10. Wan H, Wang J, Zhang Z, Cai Y, Sun B, Zhang L. High efficiency mode-locked, cylindrical vector beam fiber laser based on a mode selective coupler. *Opt Express*. 2017;25(10):11444–51.
11. Hu T, Zhong Q, Li N, Dong Y, Xu Z, Fu YH, et al. CMOS-compatible a-Si metalenses on a 12-inch glass wafer for fingerprint imaging. *Nanophotonics*. 2020;9(4):823–30.
12. Wu J, Lai Z, Zhou Y, Xie Y, Lei H, Liu D, et al. High Energy Singular Beams Generation From a Dissipative Soliton Resonance Raman Fiber Laser. *J Light Technol*. 2023;41(15):5091–6.
13. Enderli F, Feurer T. Radially polarized mode-locked Nd:YAG laser. *Opt Lett*. 2009;34(13):2030–2.
14. Li L, Zheng X, Jin C, Qi M, Chen X, Ren Z, et al. High repetition rate Q-switched radially polarized laser with a graphene-based output coupler. *Appl Phys Lett*. 2014;105(22):221103.
15. Rong Z, Han Y, Wang S, Guo C. Generation of arbitrary vector beams with cascaded liquid crystal spatial light modulators. *Opt Express*. 2014;22(2):1636–44.
16. Zhou N, Liu J, Wang J. Reconfigurable and tunable twisted light laser. *Sci Rep*. 2018;8(1):11394.
17. Lin J, Genevet P, Kats MA, Antoniou N, Capasso F. Nanostructured holograms for broadband manipulation of vector beams. *Nano Lett*. 2013;13(9):4269–74.
18. Yu P, Li J, Li X, Schuütz G, Hirscher M, Zhang S, et al. Generation of switchable singular beams with dynamic metasurfaces. *ACS Nano*. 2019;13(6):7100–6.
19. Chen J, Wan C, Zhan Q. Vectorial optical fields: recent advances and future prospects. *Sci Bull*. 2018;63(1):54–74.
20. Ismaeel R, Lee T, Oduro B, Jung Y, Brambilla G. All-fiber fused directional coupler for highly efficient spatial mode conversion. *Opt Express*. 2014;22(10):11610–9.

21. Zhang W, Huang L, Wei K, Li P, Jiang B, Mao D, et al. Cylindrical vector beam generation in fiber with mode selectivity and wavelength tunability over broadband by acoustic flexural wave. *Opt Express*. 2016;24(10):10376–84.
22. Zhou Y, Yan K, Chen R, Gu C, Xu L, Wang A, et al. Resonance efficiency enhancement for cylindrical vector fiber laser with optically induced long period grating. *Appl Phys Lett*. 2017;110(16):161104.
23. Song KY, Hwang IK, Yun SH, Kim BY. High performance fused-type mode-selective coupler using elliptical core two-mode fiber at 1550 nm. *IEEE Photon Technol Lett*. 2002;14(4):501–3.
24. Wang F, Shi F, Wang T, Pang F, Wang T, Zeng X. Method of generating femtosecond cylindrical vector beams using broadband mode converter. *IEEE Photon Technol Lett*. 2017;29(9):747–50.
25. Grosjean T, Courjon D, Spajer M. An all-fiber device for generating radially and other polarized light beams. *Opt Commun*. 2002;203(1–2):1–5.
26. Geng J, Fang X, Zhang L, Yao G, Xu L, Liu F, et al. Controllable generation of large-scale highly regular gratings on Si films. *Light Adv Manuf*. 2021;2(3):274–82.
27. Sancho-Parramon J, Bosch S. Dark modes and Fano resonances in plasmonic clusters excited by cylindrical vector beams. *ACS Nano*. 2012;6(9):8415–23.
28. Lyu W, Ma T, Yan Y, Zhang C, Chao J, Cong L, et al. Nickel Nanoparticles as Broadband Saturable Absorbers for Ultrafast Photonics. *ACS Appl Nano Mater*. 2024;7(7):8221–8.
29. Sun J, Cheng H, Xu L, Fu B, Liu X, Zhang H. Ag/MXene composite as a broadband nonlinear modulator for ultrafast photonics. *ACS Photon*. 2023;10(9):3133–42.
30. Liu X, Popa D, Akhmediev N. Revealing the transition dynamics from Q switching to mode locking in a soliton laser. *Phys Rev Lett*. 2019;123(9):093901.
31. Wang K, Zhang X, Kislyakov IM, Dong N, Zhang S, Wang G, et al. Bacterially synthesized tellurium nanostructures for broadband ultrafast nonlinear optical applications. *Nat Commun*. 2019;10(1):3985.
32. Feng J, Li X, Shi Z, Zheng C, Li X, Leng D, et al. 2D ductile transition metal chalcogenides (TMCs): novel high-performance Ag₂S nanosheets for ultrafast photonics. *Adv Opt Mater*. 2020;8(6):1901762.
33. Liu J, Li X, Xu Y, Ge Y, Wang Y, Zhang F, et al. NiPS₃ nanoflakes: a nonlinear optical material for ultrafast photonics. *Nanoscale*. 2019;11(30):14383–91.
34. Lee EJ, Choi SY, Jeong H, Park NH, Yim W, Kim MH, et al. Active control of all-fibre graphene devices with electrical gating. *Nat Commun*. 2015;6(1):6851.
35. Li N, Xu Z, Dong Y, Hu T, Zhong Q, Fu YH, et al. Large-area metasurface on CMOS-compatible fabrication platform: driving flat optics from lab to fab. *Nanophotonics*. 2020;9(10):3071–87.
36. Jia W, Gao C, Zhao Y, Li L, Wen S, Wang S, et al. Intracavity spatiotemporal metasurfaces. *Adv Photon*. 2023;5(2):026002.
37. Gu P, Cai X, Xue C, Zhang Z, Zhu Y, Du W, et al. Robust and High-Efficient Fabrication of Gold Triangles Array on Optical Fiber Tip for Laser Mode Locking. *Adv Mater Interfaces*. 2022;9(26):2200703.
38. Zhang L, Zhang H, Tang N, Chen X, Liu F, Sun X, et al. 'Plug-and-play' plasmonic metafibers for ultrafast fibre lasers. *Light Adv Manuf*. 2022;3(4):653.
39. Zhang L, Sun X, Yu H, Deng N, Qiu F, Wang J, et al. Plasmonic metafibers electro-optic modulators. *Light Sci Appl*. 2023;12(1):198.
40. Wang J, Coillet A, Demichel O, Wang Z, Rego D, Bouhelier A, et al. Saturable plasmonic metasurfaces for laser mode locking. *Light Sci Appl*. 2020;9(1):50.
41. Zhao D, Liu Y, Qiu J, Liu X. Plasmonic saturable absorbers. *Adv Photon Res*. 2021;2(8):2100003.
42. Wang B, Yu P, Wang W, Zhang X, Kuo HC, Xu H, et al. High-Q plasmonic resonances: fundamentals and applications. *Adv Opt Mater*. 2021;9(7):2001520.
43. Liang Y, Zhang H, Zhu W, Agrawal A, Lezec H, Li L, et al. Subradiant dipolar interactions in plasmonic nanoring resonator array for integrated label-free biosensing. *ACS Sensors*. 2017;2(12):1796–804.
44. Zhang L, Shang X, Cao S, Jia Q, Wang J, Yan W, et al. Optical steelyard: high-resolution and wide-range refractive index sensing by synergizing Fabry-Perot interferometer with metafibers. *Photonix*. 2024;5(1):1–17.
45. Singh N, Lorenzen J, Sinobad M, Wang K, Liapis AC, Frankis HC, et al. Silicon photonics-based high-energy passively Q-switched laser. *Nat Photon*. 2024;18:485–91.
46. Zou K, Pang K, Song H, Fan J, Zhao Z, Song H, et al. High-capacity free-space optical communications using wavelength-and mode-division-multiplexing in the mid-infrared region. *Nat Commun*. 2022;13(1):7662.
47. Nielsen MD, Mortensen NA. Photonic crystal fiber design based on the V-parameter. *Opt Express*. 2003;11(21):2762–8.
48. Koshiba M, Saitoh K. Applicability of classical optical fiber theories to holey fibers. *Opt Lett*. 2004;29(15):1739–41.
49. Mao D, He Z, Lu H, Li M, Zhang W, Xiaoqi C, et al. All-fiber radially/azimuthally polarized lasers based on mode coupling of tapered fibers. *Opt Lett*. 2018;43(7):1590–3.
50. Bozinovic N, Yue Y, Ren Y, Tur M, Kristensen P, Huang H, et al. Terabit-scale orbital angular momentum mode division multiplexing in fibers. *Science*. 2013;340(6140):1545–8.
51. Wu G, Gao S, Tu J, Shen L, Feng Y, Sui Q, et al. Mode manipulation in a ring-core fiber for OAM monitoring and conversion. *Nanophotonics*. 2022;11(21):4889–98.
52. Zhang Z, Wei W, Sun G, Zeng X, Fan W, Tang L, et al. All-fiber short-pulse vortex laser with adjustable pulse width. *Laser Phys*. 2020;30(5):055102.

Publisher's Note

Springer Nature remains neutral with regard to jurisdictional claims in published maps and institutional affiliations.